Development of a Spatially Filtered Wavefront Sensor as an Aero-Optical Measurement Technique

Luke Butler[1], Stanislav Gordeyev[2]
University of Notre Dame, Notre Dame, IN, 46556

Kyle P. Lynch[3], Daniel R. Guildenbecher[4]
Sandia National Laboratories, Albuquerque, New Mexico 87123

This paper validates the concept of a spatially filtered wavefront sensor, which uses a convergent-divergent beam to reduce sensitivity to aero-optical distortions near the focal point while retaining sensitivity at large beam diameters. This sensor was used to perform wavefront measurements in a cavity flow test section. The focal point was traversed to various spanwise locations across the test section, and the overall OPD$_{RMS}$ levels and aperture-averaged spectra of wavefronts were computed. It was demonstrated that the sensor was able to effectively suppress the stronger aero-optical signal from the cavity flow and recover the aero-optical signal from the boundary layer when the focal point was placed inside the shear region of the cavity flow. To model these measured quantities, additional collimated beam wavefronts were taken at various subsonic speeds in a wind tunnel test section with two turbulent boundary layers, and then in the cavity flow test section, where the signal from the cavity was dominant. The results from the experimental model agree with the measured convergent-divergent beam results, confirming that the spatial filtering properties of the proposed sensor are due to attenuating effects at small apertures.

I.   Introduction

As a laser beam passes through turbulent flow, aero-optical structures of fluctuating densities impose optical aberration on the beam and, among other things, will cause the beam to propagate in a different direction. This is known as beam deflection or beam jitter. For small beam diameters, Huygens principle states [1] that the beam will be deflected by an amount proportional to the 2-D gradient of optical path length (OPL), according to

$$\theta_x(t) = \frac{\partial}{\partial x} OPL(x, y, t), \, \theta_y(t) = \frac{\partial}{\partial y} OPL(x, y, t). \tag{1}$$

OPL, in turn, is an integral of the density field along the beam propagation, and is given by,

$$OPL(x, y, t) = K_{GD} \int \rho(x, y, z, t) dz, \tag{2}$$

where K_{GD} is Gladstone-Dale constant [1]. Thus, by projecting a single small-aperture laser beam through turbulent flows, wavefronts can be directly measured if the convective speed is known

---

[1] Graduate student, Department of Aerospace and Mech. Eng., AIAA Student member.
[2] Associate Professor, Department of Aerospace and Mech. Eng., AIAA Associate Fellow
[3] Senior Member of Technical Staff, Aerosciences Department, AIAA Senior member.
[4] Principal Member of Technical Staff, Diagnostic Science and Engineering Department, AIAA Senior member.

[2]. As wavefronts are proportional to the integrated density field, analysis of the time series of deflection angles informs knowledge of the underlying turbulent flow. This approach was successfully used to study boundary layers [1,2,4], shear layers [1,5,6], and flows around turrets [3,7,8].

A wavefront sensor utilizes a high-speed camera with a lenslet array, along with a collimated laser beam in the area of interest and re-imaging lenses to place the image plane of the area of interest at the location of the lenslet array. The lenslet array focuses the laser light into many small airy disks, or spots, on the camera sensor, from which the centroids are computed at each moment in time. Based on the geometry of the lenslet array, the centroid displacements are converted to local deflection angles, and integration via e.g., Southwell's method [11] yields wavefronts. One challenge with this approach is that, similar to Schlieren imaging, the measured wavefronts are line-of-sight integrated quantities. Thus, strong boundary layers and shocks often interfere with and mask

Fig. 1. Overall OPD$_{RMS}$ vs aperture size for subsonic boundary layers. From [2].

the measurement of weaker signals of interest within the flow. For spanwise-uniform flows, this problem can be addressed by collecting wavefronts in both wall-normal and spanwise directions [9]. However, many flows of interest are not spanwise-uniform, or optical access may prevent multiple views.

This paper proposes and provides preliminary validation of a spatially filtered wavefront sensor to address this challenge. The proposed method exploits the observation that when piston and tip/tilt components are removed from wavefronts, the overall level of aero-optical distortion depends on the beam aperture size relative to a spatial scale of the flow [2,10]. As shown in Figure 1, the measured aero-optical distortion is zero for an infinitely-small aperture, and increases with the aperture size. Therefore, a wavefront sensor using a converging-diverging beam should be less sensitive in the region near the focal point where the beam aperture is small, while the sensitivity is retained along the remainder of the beam. This can be useful for setups in which the laser beam goes through a region of interest and another region containing contaminating distortions, such as a boundary or shear layer near the tunnel wall.

To demonstrate the spatial filtering ability of the convergent-divergent beam wavefront sensor, this technique was used to perform measurements in a test section with a turbulent boundary layer on one side and a cavity flow on the opposite wall. The dissimilar aero-optical environments of these flows allow for testing of the spatial filtering properties of this sensor. To quantify the aero-optical environment for each type of flow, separate collimated wavefront
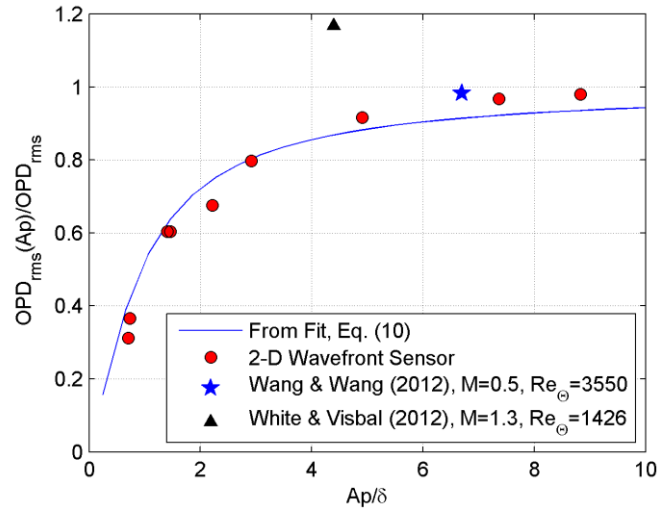
2

measurements were also performed in both the cavity flow test section and a test section with canonical boundary layers on both sides.

II.   Experimental Setup

Experiments were performed using the 99x101 mm transonic in-draft wind tunnel at the Hessert Research Laboratory at the University of Notre Dame. The wind tunnel test sections have optical quality glass installed on the sides through which the laser beam is transmitted. A variable intensity 532 nm Nd:YAG laser was expanded to 25.4 mm using a beam collimator and then further expanded to a 65 mm diameter using a -200 mm focal length lens followed by a 600 mm focal length lens, accounting for some cropping due to lens diameter. The setup for the collimated experiments is shown in Figure 2, while the setup for the convergent-divergent experiments is shown in Figure 3. Both setups used a Shack-Hartmann wavefront sensor, consisting of a Phantom v1611 high speed camera along with a 38.2 mm focal length, 0.3 mm lenslet pitch, lenslet array. Data was acquired at Mach numbers of 0.32, 0.44, and 0.55, and in most cases, the data at Mach 0.44 is presented.

Experiments were performed using a boundary layer test section that has turbulent boundary layers of δ=15.6 mm thickness on both walls, and a cavity flow test section which has a 15.6 mm boundary layer at one end and a cavity flow at the other. The streamwise length, L, of this cavity is 101.6 mm and the depth, D, is 25.4 mm. The cavity is located on the vertical wall of the test section, and the laser beam was transmitted through in the spanwise Y-direction, as shown in Figure 3. The cavity spans the entire spanwise Z-direction of the 99x101 mm test section.

For the collimated experiment, shown in Figure 2, a beam splitter was used to perform a double-pass experiment. The 65 mm return beam was contracted down to a 22 mm diameter through the beam cube and then, depending on the re-imaging setup, re-imaged to either a 17.4 mm beam or a 13.6 mm beam on the sensor. These two re-imaging setups were chosen to vary spatial and temporal resolution. A high-spatial resolution setup, acquired at 25 kHz, allows for comparison with spatially filtered data, presented later.
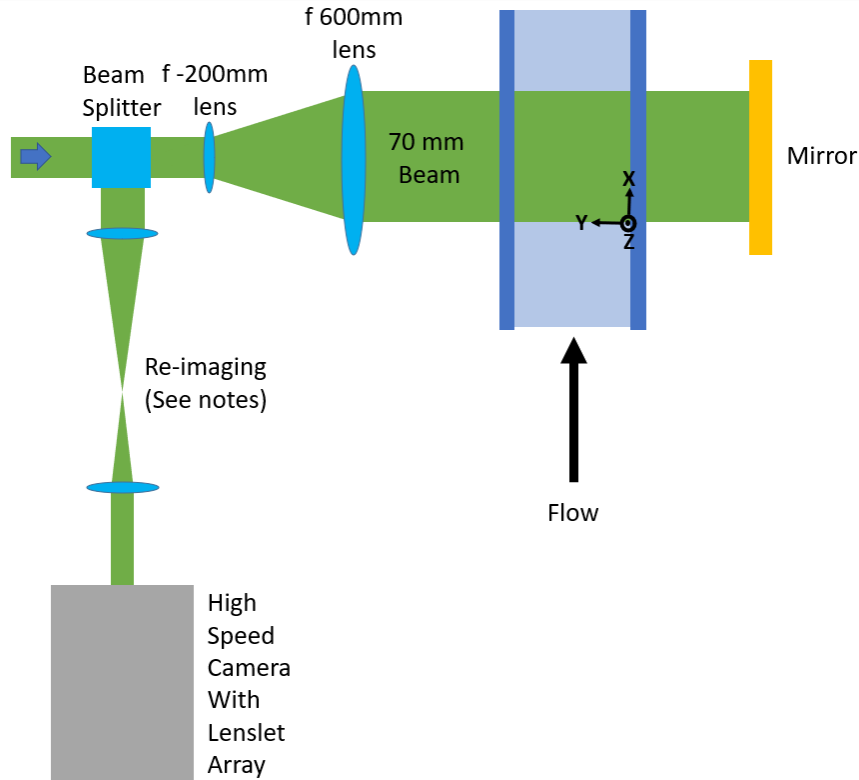
Fig. 2. Schematic of experimental setup for collimated wavefront boundary layer measurements. Note: there are two re-imaging setups: one with an f 400 mm lens followed by an f 250 lens, with 4.8x overall demagnification, sampled at 50 kHz, for better temporal resolution; and one with an f 250 lens followed by an f 200 lens, with 3.75x overall demagnification, sampled at 25 kHz, for better spatial resolution.

Figure 3 shows the schematic for the experiment with the convergent-divergent beam. Two equivalent lenses were placed at either side of the tunnel, such that the light converged to a focal point within the test section and was re-collimated thereafter. Lenses were attached to a translation stage so that the focal point could be moved to different spanwise locations within the test section. Using a pair of lenses, the outgoing beam was re-imaged onto a Shack-Hartmann wavefront sensor. In all cases, the sensor was moved to the proper location for re-imaging of the area of interest.

When the focal point was placed at locations $Y > 50.8$ mm, the wavefront sensor was positioned to re-image the shear region object plane, shown in the insert for Figure 3. At all other focal point locations for $Y \leq 50.8$ mm, the boundary layer object plane was re-imaged. This was done because if the object plane is too close the focal spot, the location of the re-imaging plane, and therefore the sensor location, approaches infinity.
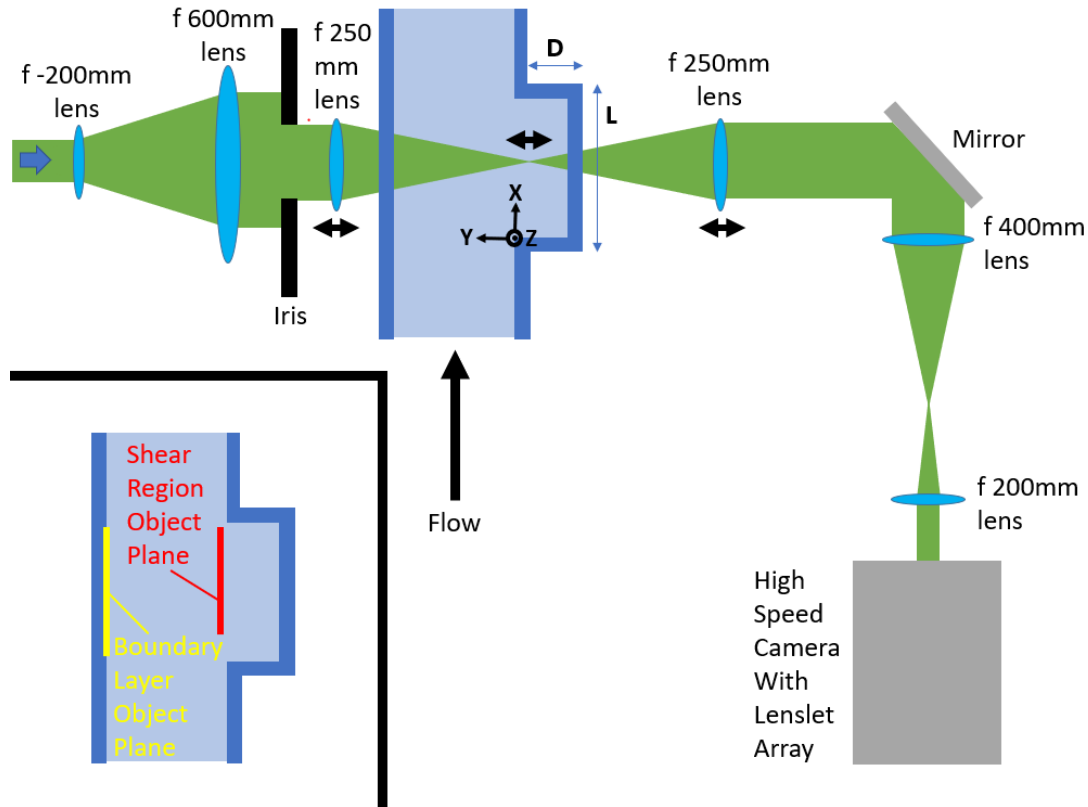
Fig. 3. Schematic of experimental setup for convergent-divergent wavefront measurements in the cavity flow test section. Focal point can be translated to any Y-location within the test section. The insert shows the locations of planes which were re-imaged onto the sensor.

III. Data Reduction

The lenslet array creates multiple focal spots on the camera sensor from which the spot centroids are extracted. Displacement of the centroids are converted to deflection angles by dividing by the lenslet focal distance of 38.2 mm. Then, the Southwell method is used to integrate the deflection angles to yield wavefronts [11]. The global tip, tilt, and piston were removed from each wavefront by fitting and subtracting a plane at each timestep. Note that for all computations, two dimmer rows of boundary points were cropped before processing to retain the best quality data.

The aperture-averaged wavefront power spectra were computed using a standard block-averaging Fourier transform in time for each point and then averaging over all spatial points. The time-averaged root-mean-square optical path difference, or temporal OPD_{RMS}, was computed by taking the standard deviation over time for each spatial point in the wavefront data. The mean OPD_{RMS} was then computed by taking the average over all the points in the array. Finally, 2D wavefront correlation maps were computed using a standard normalized unbiased autocorrelation approach.

IV.   Results and Discussion

Collimated Beam Boundary Layer Experiments

Before studying the spatial filtering properties of the converging-diverging sensor, the boundary layers and cavity flow are studied using the standard collimated wavefront setup shown in Figure 2. To demonstrate the reduction of the overall aero-optical effects at smaller apertures, the same collimated beam wavefront data was re-apertured to a series of progressively smaller apertures, instantaneous piston and tip/tilt components were removed from the resulted wavefronts, and the aperture-dependent OPD_{RMS} values were calculated. Figure 4 shows the ratio of the aperture-dependent OPD_{RMS} to the OPD_{RMS} value at the largest aperture of 61 mm, accounting for removed boundary points. The measured variation closely follows the expected trend for a canonical boundary layer [2]. As the aperture is reduced, spatial-frequencies of the measured aero-optics signal are shifted toward the low-frequency tip, tilt, and piston components. These are removed in post-processing, which effectively lowers the OPD_{RMS}.
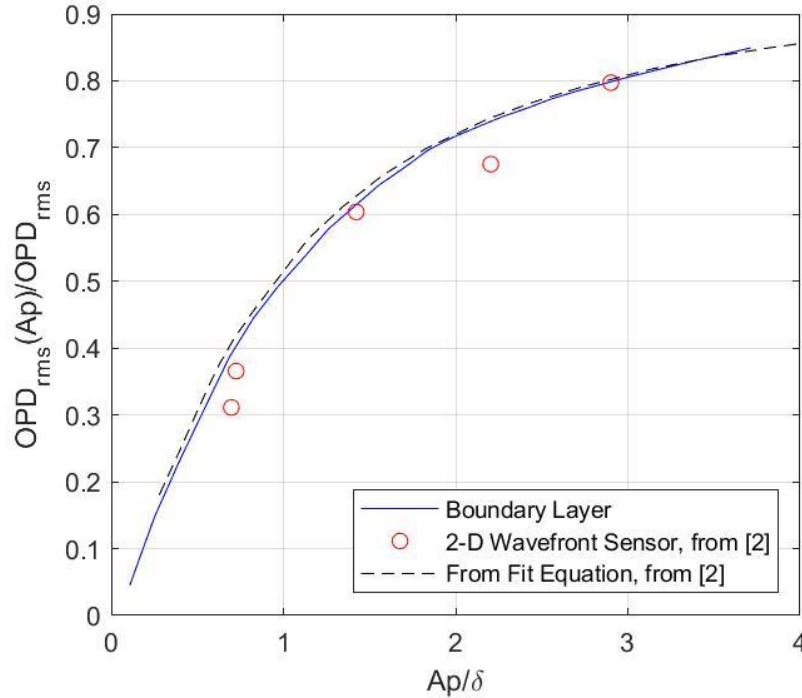

Fig. 4. Normalized OPD_RMS values vs. normalized aperture compared with canonical boundary layer results from [2]. Typical results for the Mach 0.44 boundary layer configuration are shown.

In [2], a theoretical model for OPD_{RMS} developed for canonical boundary layers and large apertures is given by,

$$OPD_{RMS} = G(M_\infty)K_{GD}\rho_\infty M_\infty^2 \delta(C_f)^{1/2} \tag{3}$$

where K_{GD} is the Gladstone-Dale constant, ρ_∞ is the free-stream density, δ is the boundary layer thickness, C_f is the coefficient of friction, M is the Mach number, and G(M)≈1−0.19M^2+0.03M^4

6

for subsonic Mach numbers. Here, the friction coefficient is estimated using the Karman Schoenherr formula from [12]. The measured values of OPD$_{RMS}$ are compared to the expected trend for the canonical boundary layers in Figure 5. The values for the Reynolds numbers Re$_\theta$ were 10.7×10^3, 13.8×10^3, and 16.8×10^3 for Mach numbers 0.32, 0.44, and 0.55, respectively. While the OPD$_{RMS}$ values are slightly higher than the linear fit for the boundary layer experiment, they follow the expected trend with varying Mach number. This confirms that the flow is similar to canonical boundary layers.
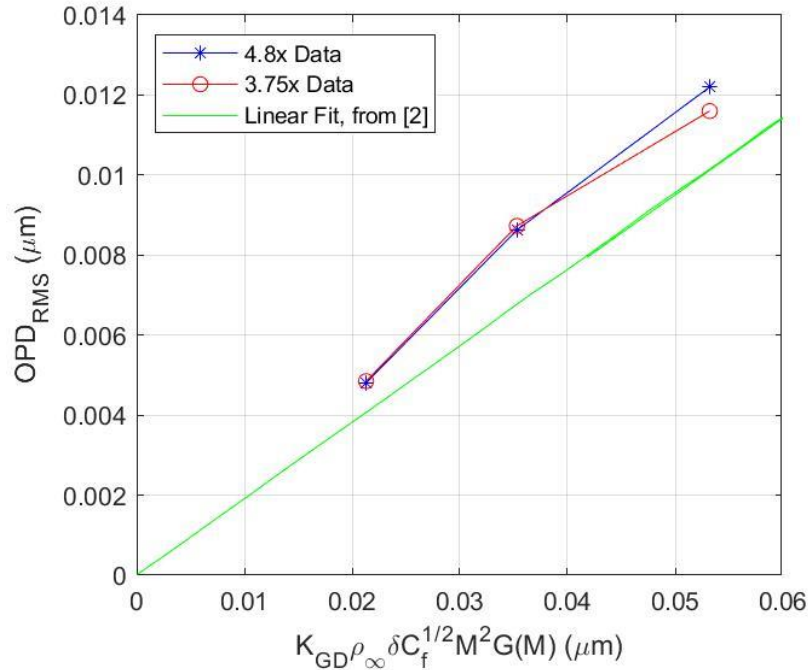

Fig. 5. OPD$_{RMS}$ values for the boundary layer compared with data from [2] at various Mach numbers.

Aperture-averaged wavefront spectra are presented for the different apertures in Figure 6. For large apertures, only the lower frequencies are attenuated. As the aperture gets smaller, higher frequencies are also attenuated. Therefore, small apertures behave as a spatial high-pass filter on the wavefronts.
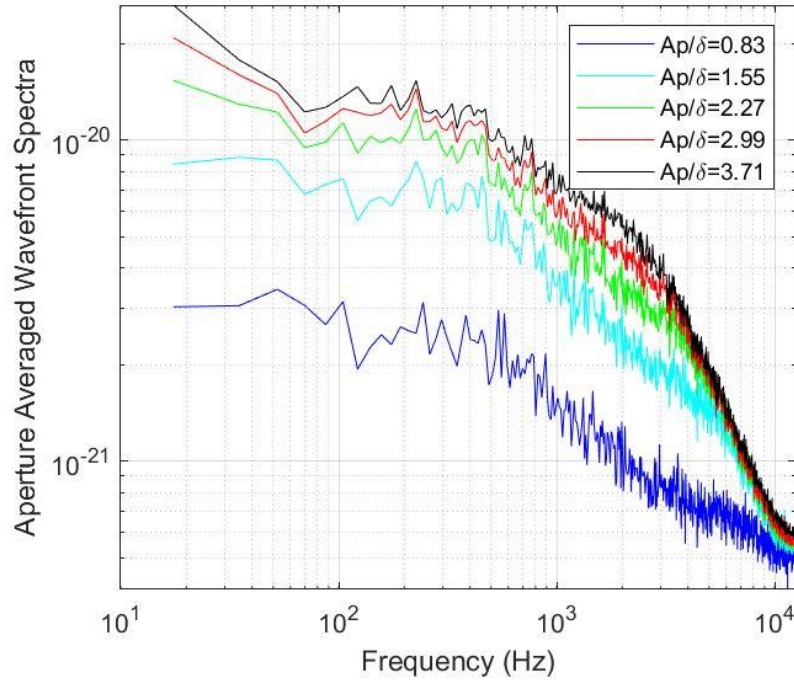
Fig. 6: Mach 0.44 boundary layer aperture-averaged wavefront spectra for different aperture sizes.

Collimated Beam Cavity Flow Experiments

Next, the more complex flow configuration within the cavity flow test section was explored. Results in this sub-section explore the use of the standard, collimated wavefront sensor shown in Figure 2, illustrating the drawbacks of such a configuration. Cavity flows are comprised of a shear region, where the fast-moving flow meets the cavity, and the cavity region [13]. The strongest aero-optic signal is due to the shear region, although the cavity affects the properties of the flow such that it is different from a shear layer alone [13]. In addition, cavity flows typically have certain natural frequencies, known as Rossiter modes, which manifest as peaks in the aero-optical spectra, although often only a subset of these modes is excited.

Table 1 provides a summary of the mean OPD$_{RMS}$ values at different Mach numbers for the collimated beam experiments with the two different flow types. The aero-optical distortions from the cavity flow are around five to six times stronger than the distortions from the boundary layer. Therefore, a measurement of the boundary layer will be heavily biased by aero-optical distortions from the cavity. Also, the ratio in OPD$_{RMS}$ values shows that the boundary layer on the opposite wall of the cavity flow test section does not add any appreciable contribution to the collimated results for the cavity flow test section, because the OPD$_{RMS}$ values from two independent flow regions are combined as a sum of squares.

8

Table 1: OPD$_{RMS}$ values for the boundary layer (BL) and cavity flow (CAV) at various Mach numbers

Mach Number	0.32	0.44	0.55
OPD$_{RMS, BL}$ (µm)	0.00483	0.008678	0.0119
OPD$_{RMS, CAV}$ (µm)	0.0229	0.0517	0.0645
OPD$_{RMS, CAV}$ / OPD$_{RMS, BL}$	4.73	5.96	5.42

As discrete frequencies are often present in cavity flows, the resulting flow structure and related aero-optical distortions will be mostly regular and periodic. This can be characterized by the two-point unbiased wavefront auto-correlation as shown in Figure 7(a). This shows that the cavity flow behaves similarly to shear layers, with alternating positive and negative vertical bands in the correlation corresponding to von Karman vortex shedding. The auto-correlation was averaged in the Z-direction, and the characteristic streamwise scale, Λ, was estimated as the distance between two minima, yielding $\Lambda = 46.1$ mm, as demonstrated by Figure 7(b).

Similar to the collimated boundary layer wavefronts, the cavity flow was re-apertured at progressively smaller apertures to evaluate the effect on OPD$_{RMS}$. Figure 8 presents the ratio of these OPD$_{RMS}$ values to the OPD$_{RMS}$ for the largest aperture of 61 mm. An increasing trend is observed, similar to the boundary layer. For comparison, the shear layer (SL) model for circular apertures from [14] is also presented. This model approximates the wavefront as a travelling wave with the single wavelength, Λ. While a single frequency model is a simplistic approximation for a cavity with multiple frequencies, qualitatively, the results are similar. Also, for the experiment to demonstrate the spatial filtering properties of the wavefront sensor with a converging-diverging beam, exact similarity to a shear layer is not significant.
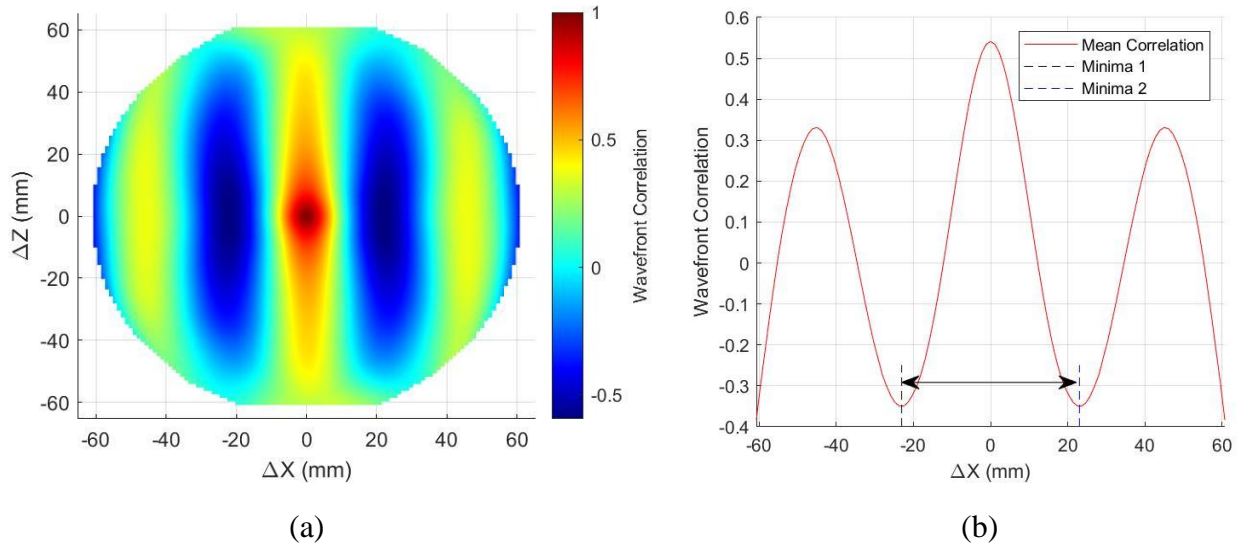

(a)   (b)

Fig. 7. (a) 2D wavefront auto-correlation map of the Mach 0.44 cavity flow. (b) ΔZ-averaged plot of the 2-D wavefront auto-correlations. The characteristic flow scale, Λ, is defined as the distance between two minima, identified by the vertical dashed lines.
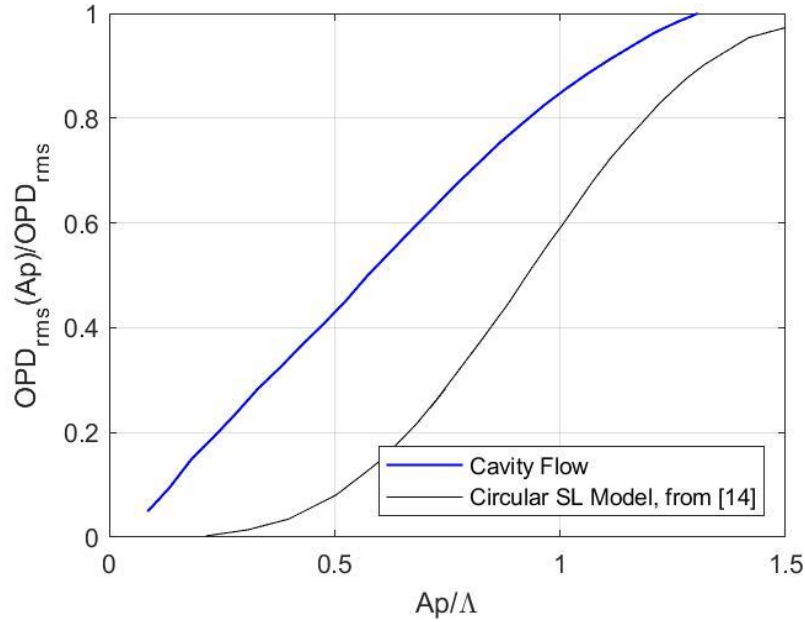
9

Fig. 8. Normalized OPDRMS values for Mach 0.44 cavity flow vs. a normalized aperture compared with expected trend for shear layers, from [14].

The aperture-averaged wavefront spectra for different apertures in the cavity flow are presented in Figure 9. The attenuating effect of reduced aperture for the cavity flow is observed. Again, as the aperture gets smaller, a greater range of frequencies, including higher frequencies, are attenuated. The vertical lines represent the expected Rossiter modes in the cavity, which are calculated using the equation below [15].

$$\frac{f_m L}{U_\infty} = \frac{m - \alpha}{\left[M_\infty \left(1 + \frac{\gamma - 1}{2} M_\infty \right)^{-1/2} + \frac{1}{\kappa} \right]} \tag{4}$$

Here, f_m is the Rossiter mode frequency, m is the mode number, L is the length of the cavity, equal to 0.1016 meters, U_∞ is the free stream velocity of 150.6 m/s, α is the phase lag, which was chosen to be zero, M_∞ is the Mach number of 0.44, γ is the ratio of specific heats of 1.4, and κ is the convective velocity, which is typically around 0.57 [13]. For this cavity flow, it was found that only even modes were excited.
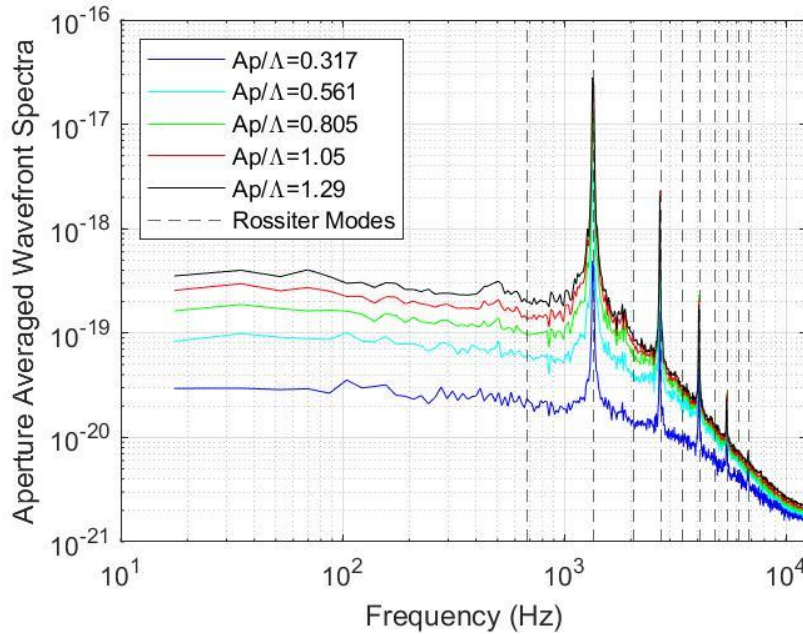
10

Fig. 9. Aperture-averaged wavefront spectra for different apertures, demonstrating the aperture-attenuating effect for the Mach 0.44 cavity flow.

Convergent-Divergent (C-D) Beam Experiments

Figures 5, 6, 8, and 9, demonstrate the basic principles of spatial filtering that are exploited in this sub-section to create a diagnostic with spatially-filtered sensitivity. With reference to Figure 3, when the focal point is far from the flow of interest and the aperture across the flow is large, the contribution to the wavefronts will primarily be preserved and aero-optical properties, such as OPD_{RMS} and the wavefront spectrum, will be largely unchanged. Conversely, when the focal point is placed at or near the corrupting flow, the aero-optical signal from it will be greatly attenuated.

To demonstrate this spatial filtering capability, the focal point of the converging-diverging experiment was moved to various *Y*-locations in the cavity flow test section. When the focal point is moved, the corresponding aperture sizes at the boundary layer region and at the shear region of the cavity flow change. The size of the effective apertures at each focal point location was calculated, assuming an ideal converging-diverging beam, and the results are shown in Figure 10. When the focal point is at the boundary layer, the boundary layer aero-optical signal should be significantly attenuated and the cavity flow signal should be recovered, and conversely, when the focal point is at the center of the shear region of the cavity flow, the cavity flow signal should be significantly reduced, and the weaker boundary layer signal should be recovered. For the convergent-divergent beam experiments, the re-imaging setup and the size of the lenslet array resulted in some cropping of the circular aperture, mostly in the Z-direction, so a cubic superellipse mask of constant shape was created that incorporated virtually all of the points. The size of the superellipse in the streamwise X-direction was the aperture size.
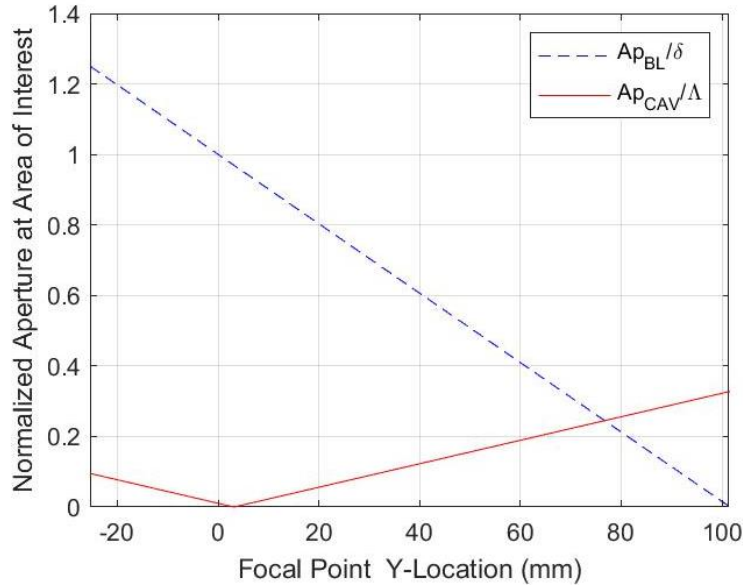
11

Fig. 10. Variation in beam aperture at the boundary layer (BL) and at the center of the shear region of the cavity flow (CAV) versus spanwise focal point location.

Figure 11 shows the aperture-averaged wavefront spectra at several focal point Y-locations across the tunnel. The vertical axis is the frequency, while the color hue represents the magnitude of the aperture averaged wavefront spectrum at that frequency. The boundary layer is located at the tunnel wall at Y = 101 mm, and the center of the shear region was estimated to be near Y = 3.2 mm. For Y > 70 mm, the aero-optical signature of the shear region was properly recovered, as witnessed by the appearance of several discrete frequencies in the spectra. For Y < 70 mm, where the focal point is closer to the shear layer, the spectra is less energetic and is expected to be more representative of the boundary layer spectrum.
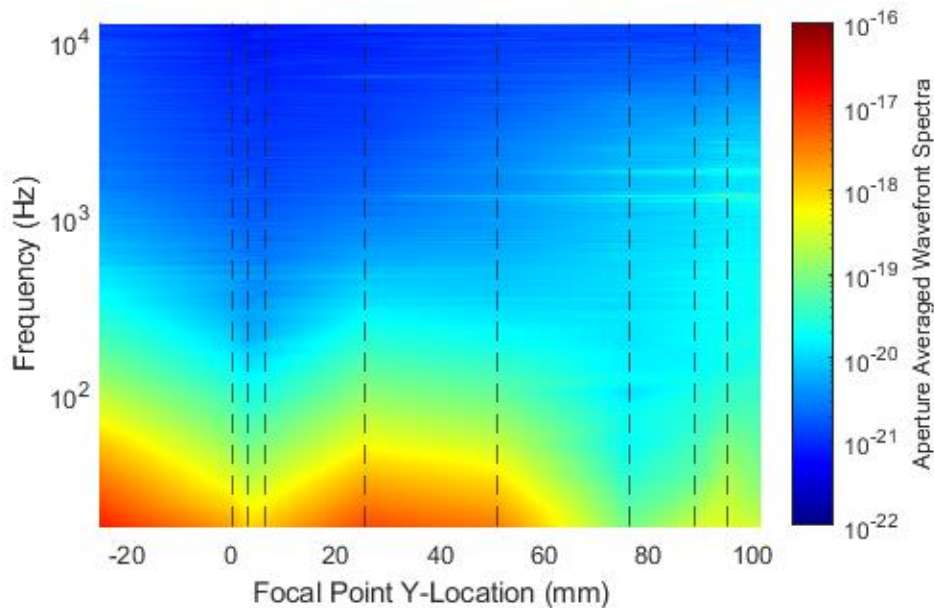

Fig. 11. Mach 0.44 cavity flow aperture-averaged wavefront spectra from convergent-divergent wavefront sensor with the focal point at various Y-locations.

12

Figure 12 shows the OPD$_{RMS}$ values from the spatially filtered wavefront sensor with the focal point at various Y-locations across the tunnel. The OPD$_{RMS}$ values are at a minimum when the focal point is located at the center of the shear region of the cavity flow at $Y = 3.2$ mm. This is consistent with greatest attenuation of the aero-optical effects occurring near the focal point.

For comparison, the experimental results were compared with a model using the collimated data from both the boundary layer and the cavity flow test sections. For simplification, the spatial extent of these flows along the laser beam was ignored, and the flows were modelled as thin phase screens. For each focal point location, the corresponding aperture sizes at the boundary layer and at the center of the shear region of the cavity flow were determined using Figure 10. Then, a mask of equal aperture to the convergent-divergent data was applied to the corresponding collimated data, and the OPD$_{RMS}$ for each flow regime was computed. Assuming that the boundary layer and the cavity flow are statistically independent, the overall signal was then determined by the sum of the squares of OPD$_{RMS}$, similar to the procedure in reference [4], and given by,

$$OPD_{RMS} = \sqrt{OPD_{RMS,BL}^2 + OPD_{RMS,CAV}^2}. \tag{5}$$

This analysis is presented in Figure 12. The values are largest at $Y = 101$ mm, where the beam is smallest inside the boundary layer, and largest inside the much stronger shear region of the cavity flow, as shown in Figure 10. Consequently, the only contribution to the modelled OPD$_{RMS}$ is from the cavity flow, which has larger aero-optical distortions. When the focal point is near the boundary layer, for $Y > 70$ mm, the modelled OPD$_{RMS}$ agrees with the convergent-divergent measurements. As the focal point moves toward the shear region, the beam size and the corresponding contribution from the boundary layer to the modelled OPD$_{RMS}$ increases, while the contribution from the shear region decreases. This demonstrates the spatial filtering of the convergent-divergent beam arrangement, where the large aero-optical effects from the shear region of the cavity flow are suppressed, while aero-optical environment from the less optically distorting boundary layer is largely unchanged.

As the shear region is modeled as a thin phase screen, when the focal point is inside of this phase screen, the beam diameter is zero and the modeled contribution from the shear region is zero. In reality, the shear region extends in the beam direction, and the beam diameter in some parts of the shear region will not be zero, albeit small. These regions with small beam diameters will still contribute to the convergent-divergent beam distortions. Therefore, the modelled OPD$_{RMS}$ should underpredict convergent-divergent OPD$_{RMS}$. This can also be observed in Figure 12. As the focal point moves toward the shear flow, the convergent-divergent measurements are consistently higher than the modelled results. Another reason for the observed deviation of the convergent-divergent data from the collimated phase screen computation is due to the rise in amplitude of the convergent-divergent signal at very low frequencies shown in Figure 11. This spectral feature will be discussed later in this paper.
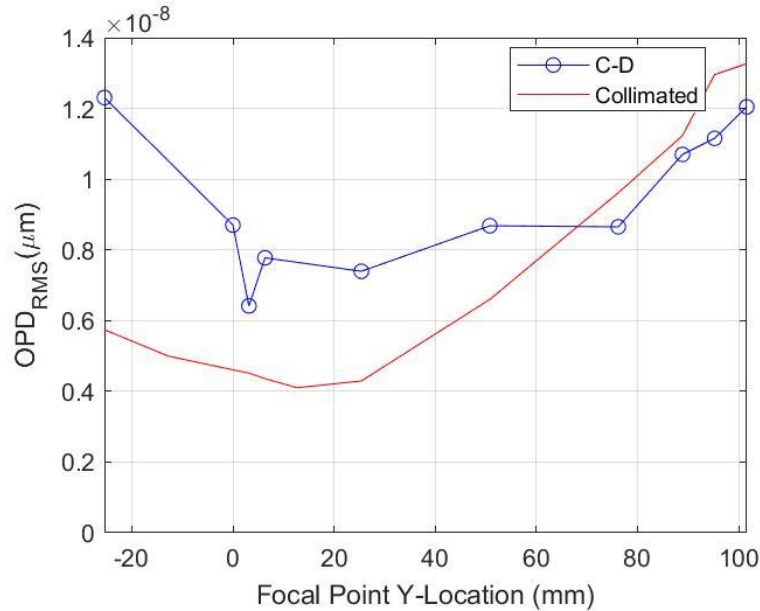
13

Fig. 12. OPD$_{RMS}$ values with the focal point at various *Y*-locations for the convergent-divergent beam (C-D) at Mach 0.44, and with the modelled values computed from the collimated data.

Following the same procedure, the power spectra for the convergent-divergent beam were modelled using the collimated data. Based on the location of the focal point, a mask of the correct aperture was applied to the collimated data from each flow configuration to determine the contribution to the aperture averaged wavefront spectrum. These boundary layer and cavity flow power spectra were then combined to determine the modelled power spectrum from the collimated phase screens.

Figure 13 shows the results for $Y = 101$ mm, with the focal point inside the boundary layer. For this *Y*-location, the beam aperture at the boundary layer wall was zero, and the convergent-divergent spectrum should be close to the shear layer spectrum. Figure 13 demonstrates close agreement across most frequencies. This shows that the sensor largely eliminates the contribution from the boundary layer while capturing the cavity flow spectrum. Note that the magnitude of cavity flow optical distortions are greater than those from the boundary layer, and would normally dominate a boundary layer signal even with a collimated setup. Therefore, this comparison is largely to verify that the sensor behaves as expected rather than to demonstrate any attenuating effects.

A notable difference is that the Rossiter modes are significantly attenuated in the convergent-divergent spectrum. One possible reason for this is uncertainty in centering of the beam along the *X*-direction of the cavity. Another difference is at frequencies below 100 Hz, where higher values are present for all the convergent-divergent spectra, which are not present in the modelled spectra. The exact source of this disagreement is not yet known, and further investigation is warranted.
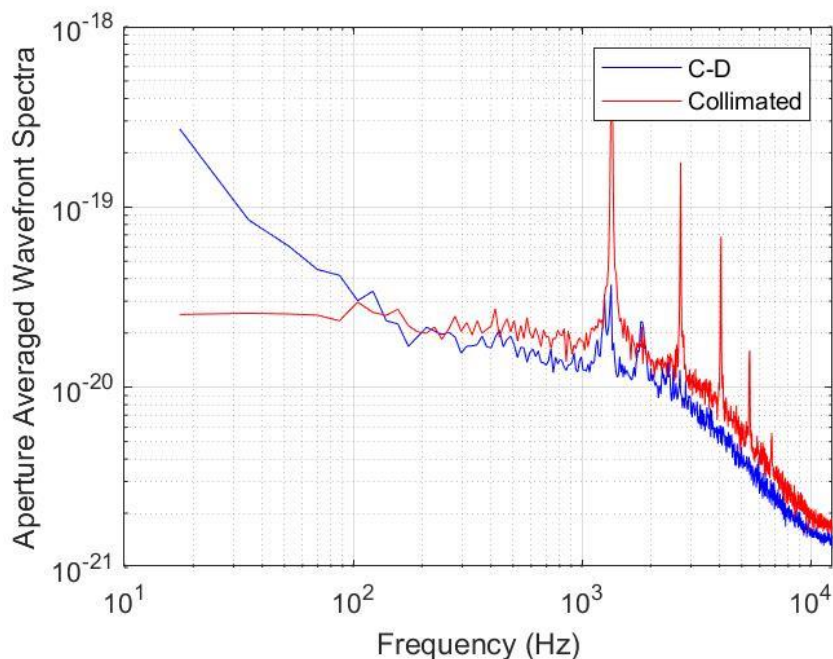
14

Fig. 13. Comparison between the spectra from convergent-divergent (C-D) beam at Mach 0.44 and the modelled spectrum using the collimated data. The *Y*-location is inside the boundary layer, at *Y* = 101 mm.

To demonstrate the attenuating effect of the spatially filtered wavefront sensor, the focal point was placed at the center of the shear region of the cavity flow. This is expected to achieve the greatest possible attenuation of the cavity flow and the best ability to recover the weaker aero-optical signal from the boundary layer. Figure 14 presents a comparison between the convergent-divergent and the modelled spectra for $Y = 3.2$ mm. Apart from the increase at low frequencies also observed in Figure 13, the convergent-divergent spectrum shows excellent agreement with the modeled spectrum computed from phase screens using the collimated data. With the focal point in the shear region, the much stronger aero-optical environment from the cavity flow is largely suppressed, and only the boundary layer distortions remain. Furthermore, the results in Figure 14 show that the contribution from the cavity flow to this wavefront signal is essentially zero when the focal point was at the center of the shear region, despite this shear region having some finite width. This indicates that the small but nonzero beam diameters near the focal point are sufficiently small to essentially filter out the entire signal for the sampled frequency range when the majority of the contamination is within a relatively narrow area such as the cavity flow shear region.
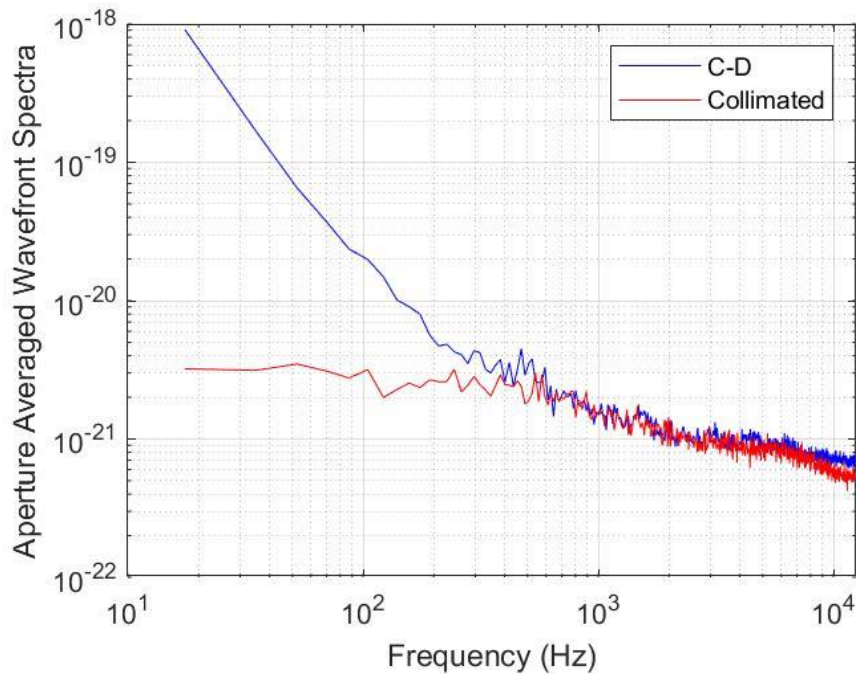
15

Fig. 14. Comparison between the spectra from convergent-divergent (C-D) beam at Mach 0.44 and the modelled spectrum using the collimated data. Focal spot location is inside the shear region of the cavity flow, at $Y = 3.2$ mm.

Finally, to test if the spatially filtered wavefront sensor can recover the correct spectrum with contributions from both the boundary layer and the cavity flow, the focal point was placed halfway between these flows near the center of the tunnel. The corresponding convergent-divergent and modelled spectra are shown in Figure 15. Apart from the rise at low frequencies below 1 kHz and a small mismatch in amplitudes of the Rossiter modes as mentioned previously, there is excellent agreement between the convergent-divergent spectrum and the modeled spectrum computed using phase screens from the collimated data.
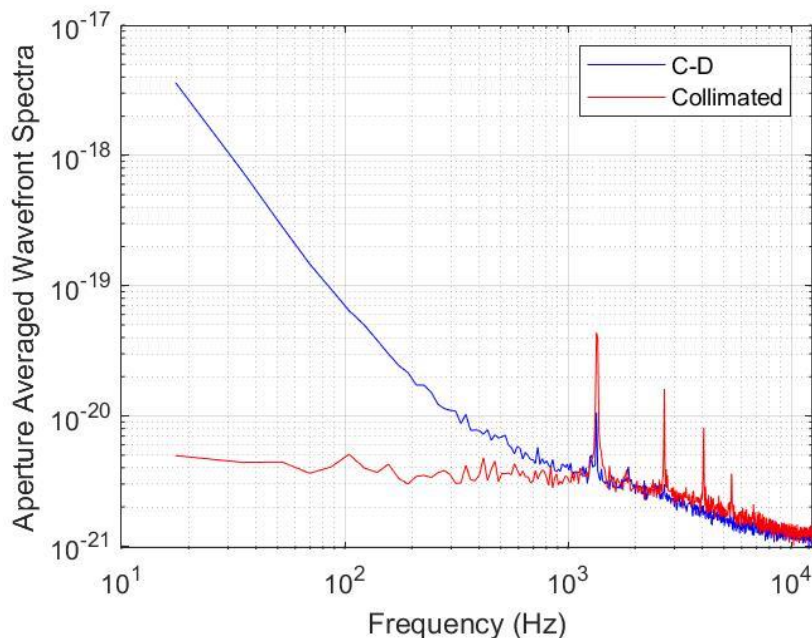
16

Fig. 15. Comparison between the spectra from convergent-divergent (C-D) beam at Mach 0.44 and the modelled spectrum using the collimated data. Focal spot location is halfway between the boundary and the shear layers, at $Y = 50.8$ mm.

Together, Figures 13-15 show that, although further investigation should be done to identify the source of low frequency contamination and ultimately eliminate it, the concept of filtering out aero-optical contributions from different areas in the flow along the beam via varying aperture sizes with a convergent-divergent beam works. When the focal point was placed at the boundary layer, the proper aero-optical statistics of the cavity flow were recovered. Similarly, when the focal point was placed at the center of the shear region of the cavity flow, the aero-optical environment of the boundary layer was recovered. Finally, with the focal point in the center of the tunnel, the combination of the contributions from each flow regime for the correct aperture sizes recreated the signal as expected.

V. Conclusions

The concept of using a convergent-divergent beam to create a spatially filtered wavefront sensor with optical attenuation near the focal point was presented and studied. This diagnostic relies on the fact that the filtering of tip, tilt, and piston components from wavefronts removes any aero-optical distortions larger than the aperture of the beam. As the beam aperture is almost zero near the focal point in a convergent-divergent beam, the contribution from the region near the focal point is removed, while the contributions from other regions are largely unaffected.

A demonstration was performed in a subsonic tunnel with two dissimilar aero-optical flows; a boundary layer at one wall and a flow over a cavity at the opposite wall. Wavefront data was collected with the focal point at various spanwise locations. In addition, traditional collimated wavefront measurements were taken in the cavity flow test section and in a separate test section with boundary layers on either side. Using the collimated beam experiments, the wavefronts were

re-apertured at progressively smaller apertures, and the aperture-related attenuating effect was confirmed in both the OPD$_{RMS}$ levels and the spectra of aero-optical distortions.

The collimated wavefront data was used to model the convergent-divergent beam results. Specifically, the collimated data from each of these experiments was apertured down to the corresponding aperture sizes of the convergent-divergent beam for each focal point *Y*-location and then combined. With the focal point at the boundary layer, the aero-optical environment of the cavity flow was recaptured, and with the focal point in the center of the shear region of the cavity flow, the aero-optical distortions related only to the boundary layer were recovered. The only significant deviations between the measured and the modelled spectra were observed at low frequencies below 1 kHz, and the exact reason for this discrepancy is currently under investigation.

Because the boundary layer distortions are much weaker than the cavity flow distortions and would normally be overridden by the stronger cavity flow if a traditional collimated beam set-up were used, the recovery of the boundary layer signal verifies the spatial filtering properties of the wavefront sensor with a convergent-divergent beam. Finally, an additional verification of this sensor was performed by placing the focal point near the center of the tunnel, and it was shown that, apart from low frequency contamination, the wavefront spectrum of the convergent-divergent beam was virtually identical to the combined contributions from both flows at opposite sides of the test section. The proposed spatially filtered wavefront sensor can be a useful tool for taking wavefront measurements with signals near the focal point greatly attenuated, allowing aero-optical distortions in the regions with large beam apertures to be correctly measured.

References
[1] S. Gordeyev, E.J. Jumper, "Physics and Measurement of Aero-Optical Effects: Past and Present," Annual Review of Fluid Mechanics, **49**, pp. 419–441, 2017

[2] S. Gordeyev, A. E. Smith, J.A. Cress and E.J. Jumper, "Experimental studies of aero-optical properties of subsonic turbulent boundary layers," *Journal of Fluid Mechanics*, **740**, pp. 214-253, 2014.

[3] S. Gordeyev, T. Hayden and E. Jumper, "Aero-Optical and Flow Measurements Over a Flat-Windowed Turret", *AIAA Journal*, **45**(*2*), pp. 347-357, 2007.

[4] S. Gordeyev, J.A. Cress, A Smith and E.J. Jumper, " Aero-optical measurements in a subsonic, turbulent boundary layer with non-adiabatic walls", Physics of Fluids, 27, 045110, 2015.

[5] Malley M, Sutton GW, Kincheloe N. 1992. Beam-jitter measurements of turbulent aero optical path differences. Appl. Opt. 31:4440–43.

[6] Fitzgerald, E., and Jumper, E. (2004). The optical distortion mechanism in a nearly incompressible free shear layer. Journal of Fluid Mechanics, 512, 153-189.

[7] N. De Lucca, S. Gordeyev, and E. Jumper, "The Study of Aero-Optical and Mechanical Jitter for Flat-Windowed Turrets", AIAA Paper, 2012-0623.

[8] B. Vukasinovic, A. Glezer, S. Gordeyev, E. Jumper and V. Kibens, "Fluidic Control of a Turret Wake: Aerodynamic and Aero-Optical Effects", AIAA Journal, Vol. 48,No, 8, pp. 1686-1699, 2010.

[9] J. Sontag and S. Gordeyev, "Non-intrusive Velocity and Density Measurements in Subsonic Turbulent Boundary Layer ", AIAA Paper 2015-3247, 2015.

[10] Siegenthaler, J., "Guidelines for adaptive-optic correction based on aperture filtration," PhD Thesis, University of Notre Dame, 2009.

[11] W. H. Southwell, "Wave-front estimation from wave-front slope measurements," Journal of the Optical Society of America, vol. 70, no. 8, pp. 998-1006, 1980.

[12] H. M. Nagib, K. A. Chauhan, and P. A. Monkewitz, "Approach to an Asymptotic State for Zero Pressure Gradient Turbulent Boundary Layers", Phil. Trans. R. Soc. A, 365, 755–770, 2007.

[13] I. A. Zilberter and J. R. Edwards, "Numerical Simulation of Aero-Optical Effects in a Supersonic Cavity Flow" AIAA Journal, Vol. 55, No. 9, pp. 3096-3108, 2017.

[14] J.P. Siegenthaler, E.J. Jumper and S. Gordeyev, "Atmospheric Propagation Vs. Aero-Optics", 46th Aerospace Science Meeting and Exhibit, Reno, Nevada, 7-10 Jan, 2008, AIAA Paper 2008-1076.

[15] Wagner, Justin, Beresh, Steven J., Casper, Katya Marie, DeMauro, Edward Paisley, and Arunajatesan, Srinivasan. "Resonance Dynamics in Compressible Cavity Flows using Time-Resolved Particle Image Velocimetry and Pressure Sensitive Paint." United States: N. p., 2017. Web. doi:10.2514/6.2017-0475.